

Integrated sensing and communications in the 3GPP New Radio: sensing limits

Santiago Fernández, Javier Giménez, Mari Carmen Aguayo-Torres, José A. Cortés

Communications and Signal Processing (ComSP) Lab, Telecommunication Research Institute (TELMA),
Universidad de Málaga, E.T.S. Ingeniería de Telecomunicación, Bulevar Louis Pasteur 35, 29010 Málaga (Spain)
{sff, jgimenezdlc, mdaguayo, jca}@uma.es

Abstract—Integrated Sensing and Communications (ISAC) is regarded as a key element of the beyond-fifth-generation (5G) and sixth-generation (6G) systems, raising the question of whether current 5G New Radio (NR) signal structures can meet the sensing accuracy requirements specified by the Third Generation Partnership Project (3GPP). This paper addresses this issue by analyzing the fundamental limits of range and velocity estimation through the Cramér–Rao lower bound (CRLB) for a monostatic unmanned aerial vehicle (UAV) sensing use case currently under consideration in the 3GPP standardization process. The study focuses on standardized signals and also evaluates the potential performance gains achievable with reference signals specifically designed for sensing purposes.

The compact CRLB expressions derived in this work highlight the fundamental trade-offs between estimation accuracy and system parameters. The results further indicate that information from multiple slots must be exploited in the estimation process to attain the performance targets defined by the 3GPP. As a result, the 5G NR positioning reference signal (PRS), whose patterns may be suboptimal for velocity estimation when using single-slot resources, becomes suitable when multislot estimation is employed. Finally, we propose a two-step iterative range and radial-velocity estimator that attains the CRLB over a significantly wider range of distances than conventional maximum-likelihood (ML) estimators, for which the well-known threshold effect severely limits the distance range over which the accuracy requirements imposed by the 3GPP are satisfied.

Index Terms—5G, 6G, Integrated sensing and communications (ISAC), accuracy, distance and speed estimation, Cramér–Rao lower bound (CRLB), maximum likelihood estimation.

I. INTRODUCTION

Integrated Sensing and Communications (ISAC) has emerged as a key paradigm in the evolution towards beyond-fifth generation (5G) and sixth generation (6G) systems, enabling wireless networks to jointly provide communication services and environmental awareness [1]. In this context, sensing refers to the capability of extracting information about the environment—such as the presence, distance, and velocity of targets—by processing reflected radio signals. Hence, the distance and speed of a target can be estimated by measuring the delay and the Doppler shift of the line-of-sight echo between the transmitter and the object [2]. This differs from the positioning functionality currently defined in 5G, where the base station (BS) transmits a reference signal that is used by the user equipment (UE) to estimate its position (which is reported back to the BS). The sensing functionality inherently combines detection and parameter estimation, and its performance is typically characterized in terms of both reliability and estimation accuracy.

The integration of sensing into cellular systems enables a wide range of applications [3] [4]. On the one hand, sensing as a service allows the network to provide environmental information to external systems, such as autonomous vehicles or smart infrastructure. On the other hand, sensing can be leveraged to improve network operation itself, enabling functionalities such as blockage detection, beam management, and proactive resource allocation. However, these benefits come at the cost of a fundamental trade-off between sensing performance and resource utilization, since sensing requires the allocation of time-frequency resources that would otherwise be used for communication.

From a system perspective, sensing can be implemented under two different operational modes: monostatic and bistatic [2]. In the former, the signal is received and analyzed by the same BS, while in the bistatic case the signal is transmitted by a BS and received and analyzed by a different one. Monostatic operation simplifies synchronization and geometry but requires in-band full-duplex capabilities with stringent self-interference cancellation [5]. Bistatic (or multi-static, in case the signal is received by more than one BS) configurations relax this requirement but introduce additional complexity in terms of synchronization, coordination, and error propagation across distributed nodes.

Within the Third Generation Partnership Project (3GPP) framework, sensing is being actively investigated as part of the evolution towards 6G, of which sensing is considered a *day-zero functionality*. The initial study item has defined a use case consisting on unmanned aerial vehicle (UAV) sensing using a monostatic configuration [6]. It has defined detection metrics, such as missed detection and false alarm probabilities, as well as estimation accuracy metrics for parameters such as target distance and velocity, which must remain below predefined thresholds with a 90% confidence level.

A key open question is whether existing 5G NR signal structures are fundamentally capable of meeting these sensing accuracy requirements. Since the achievable estimation performance is inherently limited by the structure of the transmitted signals and the allocated resources, it is essential to assess these limits from a theoretical perspective before considering specific estimation algorithms.

The Cramér–Rao lower bound (CRLB) provides a fundamental benchmark for range and velocity estimation. While widely employed in integrated sensing and communications (ISAC) applications [7]–[11], existing expressions consider neither the specific structure of 5G new radio (NR) signals nor the studied

use case [7], [8], [11], rely on channel models that yield overly complex expressions evaluable only numerically [11], or model the Doppler as a frequency shift rather than as the actual spectral compression/expansion [10].

In this work, we derive the CRLB for the UAV distance and velocity estimation under different 5G NR-based grid configurations, including standardized positioning reference signal (PRS) patterns and novel sensing-oriented designs. The presented CRLB values are employed to compute the highest accuracy that can be obtained in the estimation of the range and velocity, which are compared to the limits currently agreed in [12]. This provides insights into the fundamental trade-offs between estimation accuracy and resource utilization, and identifies the conditions under which the target sensing performance can be achieved. Furthermore, we propose a two-step iterative range and velocity estimation algorithm which attains the CRLB in a much wider range of signal-to-noise ratio (SNR) than plain maximum likelihood (ML) approaches, whose threshold effect made them inadequate to comply with the imposed requirements.

The rest of this paper is organized as follows. Section II describes the system model for the considered use case. Then, the CRLBs for velocity and range estimations are derived in Section III. The different configurations for the sensing pattern are summarized in Section IV. In Section V, the proposed two-stage iterative range and velocity estimation algorithm is presented. Numerical results and discussion are presented in Section VI. Finally, conclusions are outlined in Section VII.

II. SYSTEM MODEL

The considered use case consists of a monostatic configuration for UAV sensing, according to [6]. Since we are interested in obtaining an upper bound of the achievable sensing performance, the case where only the target whose range and speed is to be estimated is present, as illustrated in Fig. 1.

The discrete-time low-pass equivalent expression of an orthogonal frequency-division multiplexing (OFDM) signal with N subcarriers and N_{cp} samples of cyclic prefix can be expressed as

$$x_{LP}(n) = \frac{1}{N} \sum_m \sum_{k \in \mathcal{K}(m)} X_{k,m} e^{j \frac{2\pi}{N} k(n - N_{cp} - mL)} \times \omega_{TX}(n - mL), \quad (2)$$

where $X_{k,m}$ is the constellation symbol carried by the k -th subcarrier in the m -th symbol, $L = N + N_{cp}$ is the number of samples per OFDM symbol and $w_{TX}(n)$ is a rectangular window of length L . The set of active carriers used in the m -th OFDM symbol is denoted as $\mathcal{K}(m)$.

The signal $x_{LP}(t)$ is then converted from digital to analog form, frequency-shifted to f_c and converted to a real one

$$x(t) = \sqrt{2} \Re \{ x_{LP}(t) e^{j2\pi f_c t} \}, \quad (3)$$

$$y_{LP}(n) = \sqrt{\alpha_T} x_{LP}(n - \tau(t)/T_s) e^{-j(2\pi f_c \tau(t) - \phi_S)} e^{j2\pi f_c T_s n} + w_{LP}(n) = \frac{\sqrt{\alpha_T}}{N} \sum_m \sum_{k \in \mathcal{K}(m)} X_{k,m} e^{j \frac{2\pi k}{N} \left(n - \frac{\tau_d}{T_s} - \frac{2v_\phi n}{c_0} - mL - N_{cp} \right)} e^{-j \left(2\pi f_c \left(\tau_d + \frac{2v_\phi n T_s}{c_0} \right) - \phi_S \right)} \omega_{TX} \left(T_s \left(n - mL - \frac{\tau_d}{T_s} - \frac{2v_\phi n}{c_0} \right) \right) + w_{LP}(n). \quad (1)$$

where $\Re\{\cdot\}$ denotes the real part.

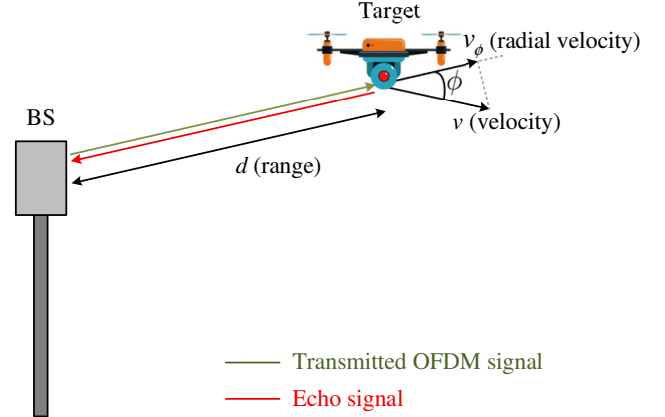


Fig. 1: Sensing use case consisting of a monostatic configuration and a single UAV.

The signal $x(t)$ is then reflected in the single sensing target (ST) located d meters away from the BS and moving at a relative radial-velocity $v_\phi = v \cos(\phi)$. Let us denote the scattering amplitude of the ST as $S = |S| e^{j\phi_S}$, which is related to the radar cross section as $\sigma_{RCS} = |S|^2$, and that is assumed to be independent of the frequency and azimuth and elevation angles. The propagation loss is modeled as free-space path loss, which assuming that the bandwidth of the transmitted signal is much smaller than the carrier frequency can be obtained as $\alpha_L = \left(\frac{c_0}{4\pi d f_c}\right)^2$ [13, Sec. 4.10-2]. Defining $\alpha_T = \alpha_L \sigma_{RCS}$, the received echo can be expressed as

$$y(t) = \sqrt{2} \Re \left\{ \sqrt{\alpha_T} x_{LP}(t - \tau(t)) e^{-j(2\pi f_c \tau(t) - \phi_S)} e^{j2\pi f_c t} \right\} + w(t), \quad (4)$$

where $w(t)$ is the noise at the receiver and $\tau(t) = 2d/c_0 + 2v_\phi t/c_0$. For simplicity of notation, $\tau_d = 2d/c_0$ is defined.

Since the transmitter and the receiver are co-located, perfect carrier and sampling synchronization can be assumed. Denoting the sampling period by $T_s = \frac{1}{N\Delta f}$, the discrete-time low-pass equivalent of the echo received at the BS can be written as in (1).

In order to compensate for part of the echo delay, the receiver is assumed to shift the discrete Fourier transform (DFT) window by $\tau_R = n_R T_s$ seconds relative to the start of the transmitted symbol. Disregarding the intercarrier interference (ICI) caused by the Doppler effect and assuming that the propagation delay is smaller than the cyclic prefix duration, the constellation symbols received at subcarrier k in the m -th OFDM symbol are then given by

$$Y_{q,m} = \sqrt{\alpha_T} X_{q,m} e^{-j2\pi \varphi_{q,m}(\tau_d, v_\phi)} + W_{q,m}, \quad (5)$$

where the noise sample in the q -th subcarrier of the m -th OFDM symbol is modeled as $W_{q,m} \sim CN(0, \sigma_w^2)$, and

$$\begin{aligned} \varphi_{q,m}(\tau_d, v_\phi) = & \underbrace{f_c \tau_d - \frac{\phi_S}{2\pi}}_{\psi} + \Delta f q (\tau_d - \tau_R) \\ & + (f_c + \Delta f q) \frac{2v_\phi}{c_0} \delta_m T_s, \end{aligned} \quad (6)$$

where Δf is the subcarrier spacing (SCS) and $\delta_m = (n_R + N_{cp} + \frac{N-1}{2} + mL)$.

The phase in (6) consists of three terms: two that depend on τ_d and one that depends on v_ϕ . Our goal is to estimate the distance to the ST and its radial-velocity from the information embedded in this phase term. In practice, no information about τ_d can be extracted from the phase term $f_c \tau_d$ because the product $f_c \tau_d \gg 1$, which causes phase ambiguity. Accordingly, both $f_c \tau_d$ and ϕ_S are grouped in the unknown parameter ψ .

It is worth to highlight that expression (6) differs from the widely used one given in [14]. In the latter, the phase shift associated to the radial speed, v_ϕ , is independent of $\Delta f q$. This is due to the more accurate modeling of the Doppler effect used in (1), which causes a compression or expansion of the signal in addition to the frequency shift considered in [14].

III. CRAMER-RAO LOWER BOUND OF RANGE AND VELOCITY

Let us now determine the CRLB of the range and radial-velocity estimation from a set of OFDM symbols with indexes $m \in \mathcal{M}$, with $M = |\mathcal{M}|$. To this end, it can be firstly observed that $Y_{q,m} \sim CN(\sqrt{\alpha_T} X_{q,m} e^{-j2\pi\varphi_{q,m}(\tau_d, v_\phi)}, \sigma_w^2)$. Since noise samples in different subcarriers and OFDM symbols are independent, the log-likelihood function (LLF) can be expressed as in (9) and the Fisher information as in (10), where it has been assumed that the constellation symbols of the sensing signals have equal amplitude, $|X_{q,m}|^2 = E_X$. Denoting the SNR in the q -th subcarrier as $\text{SNR}_q = \alpha_T E_X / \sigma_w^2$, the elements $I_{ij} = [\mathbf{I}(\tau_d, v_\phi, \psi)]_{i,j}$ are given by

$$\begin{aligned} I_{11} &= \sum_{m \in \mathcal{M}} \sum_{q \in \mathcal{K}(m)} \text{SNR}_q (\Delta f q)^2 \\ I_{12} = I_{21} &= \frac{2T_s}{c_0} \sum_{m \in \mathcal{M}} \sum_{q \in \mathcal{K}(m)} \text{SNR}_q \Delta f q (f_c + \Delta f q) \delta_m \\ I_{13} = I_{31} &= \sum_{m \in \mathcal{M}} \sum_{q \in \mathcal{K}(m)} \text{SNR}_q \Delta f q \\ I_{22} &= \left(\frac{2T_s}{c_0} \right)^2 \sum_{m \in \mathcal{M}} \sum_{q \in \mathcal{K}(m)} \text{SNR}_q (f_c + \Delta f q)^2 \delta_m^2 \\ I_{23} = I_{32} &= \frac{2T_s}{c_0} \sum_{m \in \mathcal{M}} \sum_{q \in \mathcal{K}(m)} \text{SNR}_q (f_c + \Delta f q) \delta_m, \\ I_{33} &= \sum_{m \in \mathcal{M}} \sum_{q \in \mathcal{K}(m)} \text{SNR}_q. \end{aligned} \quad (7)$$

The CRLB for the estimation of d and v_ϕ can then be

expressed as

$$\begin{aligned} \text{VAR}(\hat{d}) &\geq \frac{c_0^2}{32\pi^2} \frac{I_{22}I_{33} - I_{23}^2}{\det(\mathbf{I}(\tau_d, v_\phi, \psi))} \\ \text{VAR}(\hat{v}_\phi) &\geq \frac{1}{8\pi^2} \frac{I_{11}I_{33} - I_{13}^2}{\det(\mathbf{I}(\tau_d, v_\phi, \psi))}, \end{aligned} \quad (8)$$

where $\det(\cdot)$ denotes the determinant operator.

Assuming that all subcarriers experience the same SNR, $\text{SNR}_q = \text{SNR}$, that $f_c \gg \Delta f q$, and that all symbols use the whole set of active subcarriers for sensing purposes, $\mathcal{K}(m) = \mathcal{K}$, the CRLB can be compactly written as

$$\begin{aligned} \text{VAR}(\hat{d}) &\geq \Gamma \cdot \frac{1}{\Delta f^2} \cdot \frac{1}{\frac{1}{N_A} \sum_q q^2 - (\frac{1}{N_A} \sum_q q)^2} \\ \text{VAR}(\hat{v}_\phi) &\geq \Gamma \cdot \frac{N^2 \cdot \Delta f^2}{f_c} \cdot \frac{1}{\frac{1}{M} \sum_m \delta_m^2 - (\frac{1}{M} \sum_m \delta_m)^2}, \end{aligned} \quad (11)$$

with

$$\Gamma = \frac{c_0^2}{32\pi^2 \cdot \text{SNR} \cdot M \cdot N_A}. \quad (12)$$

As expected, the CRLB of both range and radial-velocity improves with the SNR and the number of observations $M \cdot N_A$. However, while increasing the SCS, Δf , improves the range estimation, it degrades the radial-velocity one. Increasing the carrier frequency improves the velocity estimation without affecting the range one. Interestingly, range and radial-velocity estimation improve with increasing subcarrier and symbol index variance, respectively, consistent with [15].

The CRLBs in (11) express the upper bound of the estimation process in terms of the variance. However, 3GPP has agreed to use accuracy for a given confidence level as key performance indicator (KPI) [6]. Both magnitudes can be related as follows. The accuracy of an estimator $\hat{\theta}$ for a confidence level $(1 - \alpha)$ (α is the significance level), is defined as the value of $\Delta\theta$ that fulfills

$$\text{Pr}(|\hat{\theta} - \theta| \leq \Delta\theta) = 1 - \alpha. \quad (13)$$

Assuming that $\hat{\theta}$ is normally distributed with variance and bias $\text{VAR}(\hat{\theta})$ and $\text{B}(\hat{\theta})$, respectively¹, (13) can be expressed in terms of the Gaussian Q-function, $Q(\cdot)$, as

$$1 - \alpha = 1 - Q\left(\frac{\Delta\theta - \text{B}(\hat{\theta})}{\sqrt{\text{VAR}(\hat{\theta})}}\right) - Q\left(\frac{\Delta\theta + \text{B}(\hat{\theta})}{\sqrt{\text{VAR}(\hat{\theta})}}\right), \quad (14)$$

from which $\Delta\theta$ can be obtained.

IV. SENSING PATTERNS

A. Full-slot

The upper bound in the sensing performance is attained when all active subcarriers of all the OFDM symbols in the slot are employed for this purpose. This signal pattern will be hereafter referred to as full-slot. The number of active subcarriers, N_A , is smaller than the total number of subcarriers ($N_A < N$),

¹While the CRLB is derived for unbiased estimators, we herein provide the relation for the general case of a biased estimator.

$$\Lambda(\tau_d, v_\phi, \psi) = - \sum_{m \in \mathcal{M}} \sum_{q \in \mathcal{K}(m)} \frac{1}{\sigma_w^2} (|Y_{q,m}|^2 + \alpha_T E_X + \ln(\pi \sigma_w^2)) + \frac{2\sqrt{\alpha_T}}{\sigma_w^2} \sum_{m \in \mathcal{M}} \sum_{q \in \mathcal{K}(m)} \Re \left\{ X_{q,m} e^{j2\pi \varphi_{q,m}(\tau_d, v_\phi)} Y_{q,m}^* \right\}. \quad (9)$$

$$\mathbf{I}(\tau_d, v_\phi, \psi) = \begin{bmatrix} -\mathbb{E} \left[\frac{\partial^2 \Lambda(\tau_d, v_\phi, \psi)}{\partial \tau_d^2} \right] & -\mathbb{E} \left[\frac{\partial^2 \Lambda(\tau_d, v_\phi, \psi)}{\partial \tau_d \partial v_\phi} \right] & -\mathbb{E} \left[\frac{\partial^2 \Lambda(\tau_d, v_\phi, \psi)}{\partial \tau_d \partial \psi} \right] \\ -\mathbb{E} \left[\frac{\partial^2 \Lambda(\tau_d, v_\phi, \psi)}{\partial v_\phi \partial \tau_d} \right] & -\mathbb{E} \left[\frac{\partial^2 \Lambda(\tau_d, v_\phi, \psi)}{\partial v_\phi^2} \right] & -\mathbb{E} \left[\frac{\partial^2 \Lambda(\tau_d, v_\phi, \psi)}{\partial v_\phi \partial \psi} \right] \\ -\mathbb{E} \left[\frac{\partial^2 \Lambda(\tau_d, v_\phi, \psi)}{\partial \psi \partial \tau_d} \right] & -\mathbb{E} \left[\frac{\partial^2 \Lambda(\tau_d, v_\phi, \psi)}{\partial \psi \partial v_\phi} \right] & -\mathbb{E} \left[\frac{\partial^2 \Lambda(\tau_d, v_\phi, \psi)}{\partial \psi^2} \right] \end{bmatrix}. \quad (10)$$

as defined in [16], where the maximum number of resource blocks (RBs) is determined by the signal bandwidth. The set of subcarrier indices is then given by

$$\mathcal{K}(m) = \mathcal{K} = \left\{ -\frac{N_A}{2}, \dots, \frac{N_A}{2} - 1 \right\}. \quad (15)$$

B. Positioning reference signal (PRS)

The 5G NR standard defines a set of downlink reference signals for different purposes. Among the most representative are the synchronization signal (SS), which enables the UE to detect a cell; the demodulation reference signal (DM-RS), used for downlink channel estimation; the channel state information reference signal (CSI-RS), used to assess link quality; and the PRS, which allows the UE to estimate time-of-arrival, typically using PRSs from multiple BSs [17], [18]. Among the reference signals, the PRS has important advantages for downlink sensing purposes, such as higher flexibility and density (as it admits multiple configurations) and being an always-on signal.

The mapping of PRS symbols onto the physical resource grid is primarily governed by the *comb size*, denoted as $K_{\text{comb}}^{\text{PRS}} \in \{2, 4, 6, 12\}$, which specifies the spacing between subcarriers allocated to PRS within each RB. For instance, $K_{\text{comb}}^{\text{PRS}} = 4$ implies that one out of every four subcarriers within an OFDM symbol carries PRS.

The corresponding time–frequency indices of the PRS pattern $\{q, m\}$ are defined as

$$\begin{aligned} m &= m_{\text{start}}^{\text{PRS}}, \dots, m_{\text{start}}^{\text{PRS}} + M_{\text{PRS}} - 1, \\ q &= l \cdot K_{\text{comb}}^{\text{PRS}} + ((q_{\text{offset}}^{\text{PRS}} + q') \bmod K_{\text{comb}}^{\text{PRS}}), \\ l &= 0, 1, \dots, L_{\text{PRS}} - 1, \end{aligned} \quad (16)$$

where $M_{\text{PRS}} \in \{1, 2, 4, 6, 12\}$ denotes the number of OFDM symbols within a slot allocated to PRS, $q_{\text{offset}}^{\text{PRS}} \in \{0, \dots, K_{\text{comb}}^{\text{PRS}} - 1\}$ is the frequency offset, and $L_{\text{PRS}} = N_A / K_{\text{comb}}^{\text{PRS}}$ is the number of PRS repetitions across frequency. Only the following combinations of $\{M_{\text{PRS}}, K_{\text{comb}}^{\text{PRS}}\}$ are supported in the specification,

$$\begin{aligned} \{M_{\text{PRS}}, K_{\text{comb}}^{\text{PRS}}\} \in & \{ \{1, 2\}, \{2, 2\}, \{4, 2\}, \{6, 2\}, \{12, 2\}, \\ & \{1, 4\}, \{4, 4\}, \{12, 4\}, \{1, 6\}, \{6, 6\}, \\ & \{12, 6\}, \{1, 12\}, \{12, 12\} \} \end{aligned} \quad (17)$$

However, in order to keep the overhead constant among configurations, only the cases in which $K_{\text{comb}}^{\text{PRS}} = M_{\text{PRS}}$ are employed.

The index q' in (16) depends on the relative symbol index $(m - m_{\text{start}}^{\text{PRS}})$ and $K_{\text{comb}}^{\text{PRS}}$, as summarized in Table I.

TABLE I: Value of q' for a given $(m - m_{\text{start}}^{\text{PRS}})$ and $K_{\text{comb}}^{\text{PRS}}$

$K_{\text{comb}}^{\text{PRS}}$	Relative index of the m -th symbol within the time slot											
	$(m - m_{\text{start}}^{\text{PRS}})$											
	0	1	2	3	4	5	6	7	8	9	10	11
2	0	1	0	1	0	1	0	1	0	1	0	1
4	0	2	1	3	0	2	1	3	0	2	1	3
6	0	3	1	4	2	5	0	3	1	4	2	5
12	0	6	3	9	1	7	4	10	2	8	5	11

For illustrative purposes, Fig. 2 depicts example patterns corresponding to the four possible comb sizes of the PRS within a slot. While only three RBs are shown, the PRS pattern covers the whole set of active carriers. For simplicity, it has been assumed that $m_{\text{start}}^{\text{PRS}} = 0$ and $q_{\text{offset}}^{\text{PRS}} = 0$. Under these assumptions, the indices in (16) reduce to

$$\begin{aligned} m &= 0, 1, \dots, M_{\text{PRS}} - 1, \\ q &= q' + l \cdot K_{\text{comb}}^{\text{PRS}} - \frac{N_A}{2}, \\ l &= 0, 1, \dots, L_{\text{PRS}} - 1, \end{aligned} \quad (18)$$

where the additional term $-\frac{N_A}{2}$ centers the subcarrier indices around zero. As seen, each OFDM symbol m is associated with a distinct subset of PRS subcarriers, $\mathcal{K}(m)$.

C. DDRS

Since PRS signals were not designed for sensing purposes, they have some drawbacks when used for this application. For instance, each carrier is used only once in each time slot, which hinders speed estimation. Similarly, for $K_{\text{comb}}^{\text{PRS}} = 2$, the two symbols used in each time slot are consecutive, which also yields poor performance when speed is estimated using the PRS resources of a single slot. This can be explained in terms of the CRLB in (11), where the variance of the symbol indices used in the estimation is extremely small.

To assess whether better sensing performance may be obtained with specially designed patterns, we here propose a new reference signal, which will be referred to as Doppler-delay reference signal (DDRS), to which the following design constraint are imposed. First, it must have a regular grid, using the same resource elements (REs) in all OFDM symbols. Hence, the employed frequency and time comb sizes, $K_{\text{comb}}^{\text{DDRS}}$ and $M_{\text{comb}}^{\text{DDRS}}$ respectively, differ from those used in PRS. Second, the spacing between symbols with DDRS resources should be

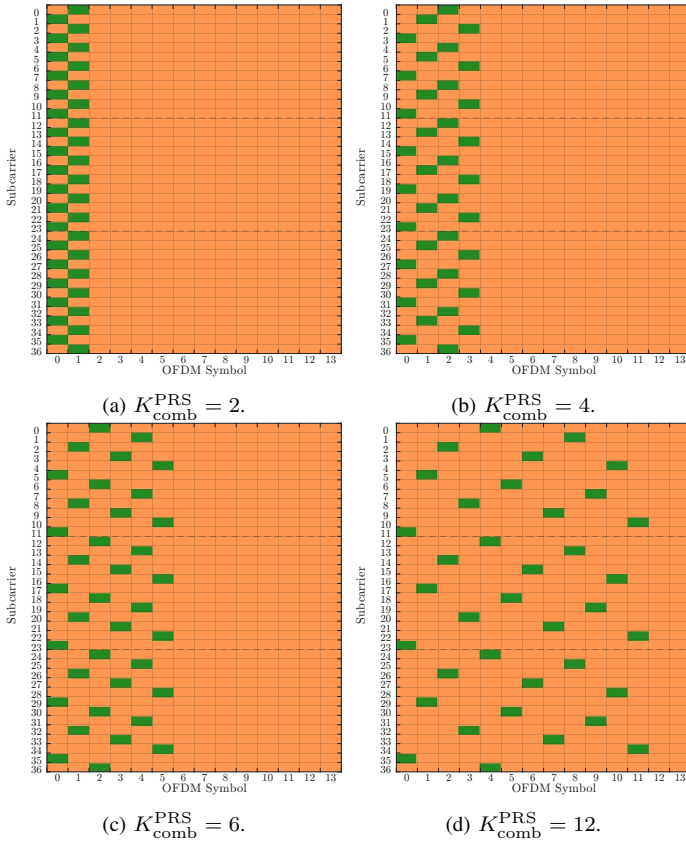


Fig. 2: Example of PRS patterns with the same overhead. The green resource elements are the ones for sensing, the orange ones are used for other purposes.

equally (or almost) spaced. Finally, DDRS must have the same overhead as the PRS.

Denoting the number of OFDM symbols per time slot as $M_{\text{OFDM}}^{\text{TS}}$, the time-frequency indices of the DDRS patterns $\{q, m\}$ are given by

$$\begin{aligned} m &= m_{\text{start}}^{\text{DDRS}} + \ell M_{\text{comb}}^{\text{DDRS}}, \\ \ell &= 0, 1, \dots, M_{\text{DDRS}} - 1, \\ q &= l \cdot K_{\text{comb}}^{\text{DDRS}}, \\ l &= 0, 1, \dots, L_{\text{DDRS}} - 1, \end{aligned} \quad (19)$$

where $M_{\text{comb}}^{\text{DDRS}} = \left\lfloor \frac{M_{\text{OFDM}}^{\text{TS}}}{K_{\text{comb}}^{\text{DDRS}}} \right\rfloor$, with $\lfloor \cdot \rfloor$ corresponding to the floor operation, $L_{\text{DDRS}} = N_A / K_{\text{comb}}^{\text{DDRS}}$ is the number of DDRS repetitions across frequency and $M_{\text{DDRS}} \in \{2, 4, 6, 7, 12, 14\}$ denotes the number of OFDM symbols within a slot allocated to DDRS.

In order to keep the overhead constant and equal to the PRS cases, the following configurations, denoted as $\{M_{\text{DDRS}}, K_{\text{comb}}^{\text{DDRS}}\}$, are supported,

$$\{M_{\text{DDRS}}, K_{\text{comb}}^{\text{DDRS}}\} \in \{\{2, 2\}, \{4, 4\}, \{6, 6\}, \{7, 7\}, \{12, 12\}, \{14, 14\}\}, \quad (20)$$

Fig. 3 shows the defined DDRS patterns. All configurations have the same overhead as the ones of the PRSs in Fig. 2: 7.14%.

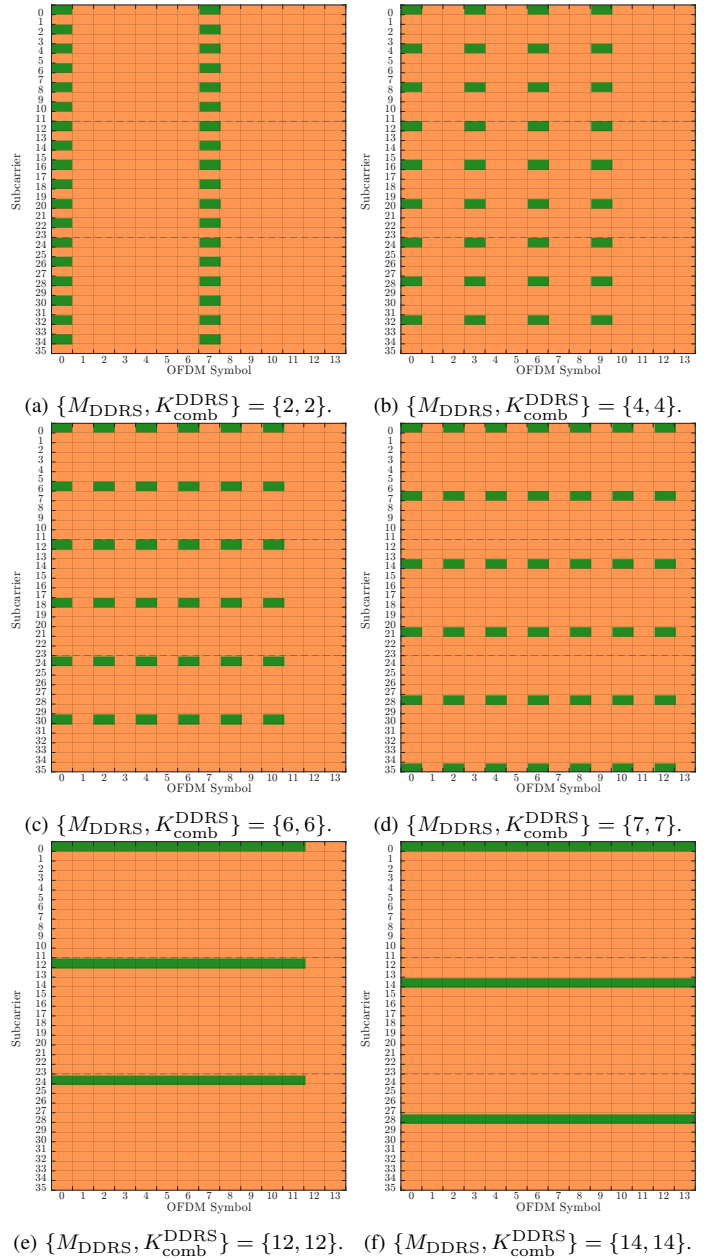


Fig. 3: Patterns of the proposed DDRS signal for sensing purposes.

It is worth noting that the configurations $\{12, 12\}$ and $\{14, 14\}$ have the same symbol separation, $M_{\text{comb}}^{\text{DDRS}} = 1$, but the latter occupies all the symbols within a slot. The same applies to the configurations $\{6, 6\}$ and $\{7, 7\}$, where $M_{\text{comb}}^{\text{DDRS}} = 2$, although the latter does not cover all the symbols within the slot.

V. RANGE AND VELOCITY ML ESTIMATORS

In this section we derive range and speed estimators for the signal in (5) and the full-slot sensing pattern, hence, $\mathcal{K}(m) = \mathcal{K}$. Since the range and velocity information is embedded in the phase of the received constellation symbol, let us define

$$Z_{q,m} = Y_{q,m}^* X_{q,m} = \sqrt{\alpha_{\text{T}}} E_X e^{j2\pi\varphi_{q,m}(\tau_d, v_\phi)} + W'_{q,m}, \quad (21)$$

with $\varphi_{q,m}(\tau_d, v_\phi)$ as given in (6) and $W'_{q,m} = X_{q,m}W_{q,m}^*$.

In order to estimate the radial-velocity, it can be observed that $\varphi_{q,m}(\tau_d, v_\phi)$ can be expressed as

$$\varphi_{q,m}(\tau_d, v_\phi) = f_{v_\phi} m + \beta_q, \quad (22)$$

where

$$\begin{aligned} f_{v_\phi} &= (f_c + \Delta f q) \frac{2v_\phi}{c_0} LT_s, \\ \beta_q &= \Delta f q (\tau_d - \tau_R) \\ &+ (f_c + \Delta f q) \frac{2v_\phi}{c_0} \left(n_R + N_{cp} + \frac{N-1}{2} \right) T_s + \psi. \end{aligned} \quad (23)$$

Since v_ϕ can be positive or negative, the span of normalized frequencies that can be unambiguously determined is $f_{v_\phi} \in [-1/2, 1/2)$. Hence, assuming that $f_c \gg \Delta f N_A/2$, the range of velocities that can be estimated unambiguously is $v_\phi \in [-v_\phi^{\max}, v_\phi^{\max})$, with

$$v_\phi^{\max} = \frac{c_0 N \Delta f}{4 f_c L}. \quad (24)$$

The ML estimator of f_{v_ϕ} from $Z_{q,m}$, assuming that both α_T and β_q are unknown, can be obtained as in [19, Eq. (7.66)]. These N_A estimates, one for each $q \in [-N_A/2, N_A/2 - 1]$, can then be averaged to obtain a single estimate of v_ϕ . However, the estimates obtained with this procedure suffer from the well-known threshold effect [20], which severely limits the range of SNR values over which it attains the CRLB. To extend this range, the noise has to be reduced before the estimation.

The following two-step iterative process can be employed to achieve this end. First, a coarse estimate of the radial-velocity, \hat{v}_ϕ^c , is obtained from the frequency-averaged value of $Z_{q,m}$ as

$$\begin{aligned} \bar{Z}_m^c &= \frac{1}{N_A} \sum_{q=-N_A/2}^{N_A/2-1} Z_{q,m} = \sqrt{\alpha_T} E_X \underbrace{\frac{1}{N_A} \frac{\sin(\pi \gamma \tau_d N_A)}{\sin(\pi \gamma \tau_d)}}_{D_{N_A}(2\pi \gamma \tau_d)} \\ &\times e^{j2\pi(F_{v_\phi}^c m + \eta^c)} + \bar{W}_m^c, \end{aligned} \quad (25)$$

where $\bar{W}_m^c \sim CN(0, \sigma_w^2/N_A)$, $D_{N_A}(x)$ denotes the Dirichlet kernel with argument

$$\gamma \tau_d = \Delta f \left(\tau_d - \tau_R + \frac{2v_\phi}{c_0} \delta_m T_s \right), \quad (26)$$

and where the frequency $F_{v_\phi}^c$ and η^c are given by

$$\begin{aligned} F_{v_\phi}^c &= \frac{2v_\phi}{c_0} LT_s \left(f_c - \frac{\Delta f}{2} \right), \\ \eta^c &= \left(f_c - \frac{\Delta f}{2} \right) \times \left(\tau_d + \frac{2v_\phi}{c_0} \left(n_R + N_{cp} + \frac{N-1}{2} \right) T_s \right) \\ &+ \Delta f \tau_R / 2 - \frac{\phi_S}{2\pi}. \end{aligned} \quad (27)$$

A coarse estimate of the radial-velocity, \hat{v}_ϕ^c , is then obtained by firstly computing the ML estimate of $F_{v_\phi}^c$ (η^c is unknown) as [19, Eq. (7.66)]

$$\hat{F}_{v_\phi}^c = \underset{f}{\operatorname{argmax}} \left\{ \left| \sum_{m=0}^{M-1} \bar{Z}_m^c e^{-j2\pi f m} \right|^2 \right\}, \quad (28)$$

which can be implemented by means of a DFT-based periodogram and a subsequent fine search using a numerical method [21], and then computing

$$\hat{v}_\phi^c = \frac{\hat{F}_{v_\phi}^c c_0}{2(f_c - \Delta f/2) LT_s}. \quad (29)$$

Since the noise variance in \bar{Z}_m^c is N_A times lower than in $Z_{q,m}$, the threshold effect is displaced to lower SNR values by $10 \log_{10}(N_A)$ (dB). However, the amplitude of \bar{Z}_m^c depends on the range of the ST by means of the Dirichlet kernel $D_{N_A}(2\pi \gamma \tau_d)$. This makes the actual SNR in (25) to vary periodically with the range of the ST. This problem will be corrected in the second phase of the algorithm.

Next, the coarse estimate of the range, \hat{d}^c is obtained. To this end, the terms associated to the radial-velocity in $Z_{q,m}$ are eliminated as

$$H_{q,m}^c = Z_{q,m} e^{-j2\pi(f_c + \Delta f q) \frac{2\hat{v}_\phi^c}{c_0} \delta_m T_s} + W_{q,m}''', \quad (30)$$

where $W_{q,m}''' = X_{q,m}W_{q,m}^* e^{-j2\pi(f_c + \Delta f q) \frac{2\hat{v}_\phi^c}{c_0} \delta_m T_s}$. In order to mitigate the threshold effect in the range estimation, a time averaging of $H_{q,m}^c$ is performed. Assuming perfect estimation of the radial-velocity, this yields

$$\bar{H}_q^c = \frac{1}{M} \sum_{m=0}^{M-1} H_{q,m}^c = \sqrt{\alpha_T} E_X e^{j2\pi \psi} e^{j2\pi \Delta f (\tau_d - \tau_R) q} \overbrace{e^{j2\pi F_d^c q}}^{F_d^c} + \bar{W}_q^c, \quad (31)$$

where $\bar{W}_q^c \sim CN(0, \sigma_w^2/M)$.

The ML estimate of F_d^c is then obtained from the observations H_q^c as

$$\hat{F}_d^c = \underset{f}{\operatorname{argmax}} \left\{ \left| \sum_{q=0}^{N_A-1} H_q^c e^{-j2\pi f q} \right|^2 \right\}, \quad (32)$$

and the coarse range estimate as

$$\hat{d}^c = \frac{\hat{F}_d^c}{\Delta f} + \tau_R. \quad (33)$$

The range of the ST, d , is a positive value, so the span of normalized frequency, f , where the maximum of the periodogram in (32) can be determined without ambiguity is $f \in [0, 1)$. In consequence, the maximum range that can be unambiguously estimated is given by

$$d_{\max} = \frac{c_0}{2} \left(\frac{1}{\Delta f} + \tau_R \right). \quad (34)$$

Now, in order to obtain a refined estimate of the radial-velocity, the range dependence in $Z_{q,m}$ can be eliminated, which removes the Dirichlet kernel that appeared in the averaging of $Z_{q,m}$ performed to mitigate the threshold effect. To this end,

$$\begin{aligned} \bar{Z}_m^r &= \frac{1}{N_A} \sum_{q=-N_A/2}^{N_A/2-1} Z_{q,m} e^{-j2\pi \Delta f q (2\hat{d}^c/c_0 - \tau_R)} \\ &= \sqrt{\alpha_T} E_X e^{j2\pi(F_{v_\phi}^r m + \eta^r)} + \bar{W}_m^r, \end{aligned} \quad (35)$$

The ML estimate of $F_{v_\phi}^r$ is now computed analogously to (28), and a refined version of the radial-velocity, \hat{v}_ϕ^r , is obtained as in (29).

Finally, a refined version of the range estimate, \hat{d}^r , is obtained. To this end, the effect of v_ϕ in $Z_{q,m}$ is firstly compensated as in (30), yielding $H_{q,m}^r$, whose time-averaged value, \overline{H}_q^r , is obtained as in (31). Finally, \hat{d}^r is obtained proceeding analogously to (32) and (33).

Algorithm V.1 Two-step iterative range and speed estimation algorithm

First iteration

- 1: Compute $Z_{q,m}$ from $Y_{q,m}$ as in (21)
- 2: Calculate \overline{Z}_m by averaging $Z_{q,m}$ over the active subcarriers as in (25)
- 3: Obtain a coarse estimate of the radial-velocity, \hat{v}_ϕ^c , from \overline{Z}_m^c using (28) and (29)
- 4: Eliminate the velocity terms in $\varphi_{q,m}(\tau_d, v_\phi)$ by computing $H_{q,m}^c$ as in (30)
- 5: Obtain a coarse estimate of the range, \hat{d}^c , from \overline{H}_q^c in (31) using (32) and (33)

Second iteration

- 6: Eliminate the range terms in $Z_{q,m}$ and compute its time-averaged value, \overline{Z}_m^r , as in (35)
 - 7: Obtain a refined estimate of the radial-velocity, \hat{v}_ϕ^r , from \overline{Z}_m^r analogously to (28) and (29)
 - 8: Eliminate the velocity terms in $\varphi_{q,m}(\tau_d, v_\phi)$ by computing $H_{q,m}^r$ and obtaining its frequency-averaged value, \overline{H}_q^r , analogously to (31)
 - 9: Obtain a refined estimate of the range, \hat{d}^r , from \overline{H}_q^r proceeding as in (32) and (33)
-

As mentioned, the employed ML estimators in (28) and (32) can be implemented by means of a DFT and a subsequent refinement using a numerical method. The size of the DFT, denoted as N_{per} , determines the resolution of the estimates, as the refinement is carried out around a normalized frequency constrained to a discrete set. Since the span of $F_{v_\phi} \in [-1/2, 1/2)$ and $F_d \in [0, 1)$ is equally spaced divided into N_{per} points, i.e., $\Delta F = 1/N_{\text{per}}$, the following velocity and range resolutions are obtained under the assumption that $f_c \gg \Delta f N_A/2$

$$\begin{aligned} \Delta v_\phi &= \frac{c_0 N \Delta f}{2 f_c N_{\text{per}} L} \\ \Delta d &= \frac{c_0}{2 N_{\text{per}} \Delta f} \end{aligned} \quad (36)$$

VI. NUMERICAL RESULTS AND DISCUSSION

This section shows the highest accuracy that can be achieved in the range and radial-speed estimation of an UAV using monostatic sensing. Next, the suitability of the PRS for sensing purposes is evaluated and compared against the performance of the proposed DDRS pattern, to assess whether the introduction of a new sensing-oriented reference signal is justified, or whether the improvements reported for other seemingly better patterns are not practically significant. Finally, since the aforementioned results are obtained by means of the CRLB, but there is no guarantee that an efficient estimator can be obtained for the considered problem, we show that the performance given by the two-step iterative estimator proposed in Section V is

efficient and compare it to the performance of a plain ML estimator.

In all cases, the accuracy of the range and radial-velocity is obtained for estimators that use sensing resources from a number of slots ranging from 1 to 20. Increasing the number of slots used in the estimation improves performance at the cost of an increased complexity, in particular the memory required to store the complex values $Y_{q,m}$ to be used by the estimator.

A. System parameters

This work uses the system parameters defined in [6] for the considered use case and that are summarized in Table II.

TABLE II: System parameters

Parameter	Description	Value
μ	Numerology index	1
f_c	Carrier frequency	4 GHz
Δf	SCS	30 kHz
BW	Channel bandwidth	100 MHz
N	Number of carriers	4096
N_{cp}	Cyclic prefix (samples)	288 samples
T_s	Sampling period	8.14 ns
N_{RB}	Number of active RBs	273
N_A	Number of active subcarriers	3276

The radar cross section (RCS) is modeled according to [22, Sec. 7.9.2.1 (model 1)], which states that it can be expressed as the product of three terms, $\sigma_{\text{RCS}} = \sigma_{\text{M}} \sigma_{\text{D}} \sigma_{\text{S}}$, where $\sigma_{\text{M}} = -12.81$ dBsm is deterministic, $\sigma_{\text{D}} = 1$ when it is independent of the angle of incidence, and σ_{S} is a log-normal random variable such that $10 \log(\sigma_{\text{S}}) \sim \mathcal{N}(\mu_{\sigma_{\text{S,dB}}}, \sigma_{\sigma_{\text{S,dB}}}^2)$, where the mean and the variance are related as

$$\mu_{\sigma_{\text{S,dB}}} = -\frac{\ln(10)}{20} \sigma_{\sigma_{\text{S,dB}}}^2, \quad (37)$$

with $\sigma_{\sigma_{\text{S,dB}}} = 3.74$ dB for small UAVs.

The inter-BS distance of 500 m agreed in [6] is assumed, which leads to a maximum coverage distance of roughly 290 m. Since the ST can be up to 300 m above the BS, the maximum range is just below 420 m. Hence, the accuracy for STs located at a maximum distance of 440 m is evaluated. According to [23], a maximum speed of 50 m/s (180 km/h) is considered.

The KPIs defined in [12] for the considered use case are given in Table III. Regarding range accuracy, since the distance d considered in this work includes both horizontal and vertical components, a 10 m accuracy requirement is imposed on d to ensure compliance in all cases. Interestingly, the values in Table III limit the maximum number of slots that can be used in the estimation. For instance, in 400 slots (0.2 s), a ST moving at 50 m/s the ST has displaced 10 m (the accuracy limit) from its position. Fortunately, a lower number of slots is actually required to meet the requirements, as it will be shown.

B. Sensing resolution and maximum values

Expressions (24) and (34) gave the maximum radial-velocity and range values that can be unambiguously estimated, while expression (36) provided the resolution that can be achieved when estimating d and v_ϕ using an N_{per} -DFT. For illustrative purposes, Table IV reports the maximum unambiguous values for range and velocity obtained using the system parameters in Table II. Similarly, Table V provides the attainable resolution for different values of N_{per} . Note that the indicated limit for range estimation corresponds to the scenario where $\tau_R = 0$, i.e., frame synchronization is not performed. Otherwise, larger ranges can, in principle, be estimated without ambiguity. However, in practice the maximum range is constrained by the sensitivity of the receiver.

C. Accuracy assessment

First, accuracy values given by (14) using the variance given by the CRLB in (11) for the full-slot pattern and the confidence levels in Table III are presented. Fig. 4 shows the results obtained when the estimation is computed over 1, 2, 4, and 20 time slots. As seen, the distance accuracy requirement is easily satisfied with a single time slot, whereas at least two time slots are necessary to meet the velocity accuracy requirement.

As expected, lower performance is obtained when using PRSs. Fig. 5 shows the accuracy bounds (derived from the CRLB) when the range and radial-velocity are estimated over the PRS resources from 1, 4 and 20 time slots. It can be observed that a single time slot is more than sufficient to meet the distance accuracy requirement, however, more than 4 time slots are now required to meet the velocity accuracy requirements. In practice, the performance is independent of

TABLE III: KPIs adopted for evaluation purpose of NR ISAC.

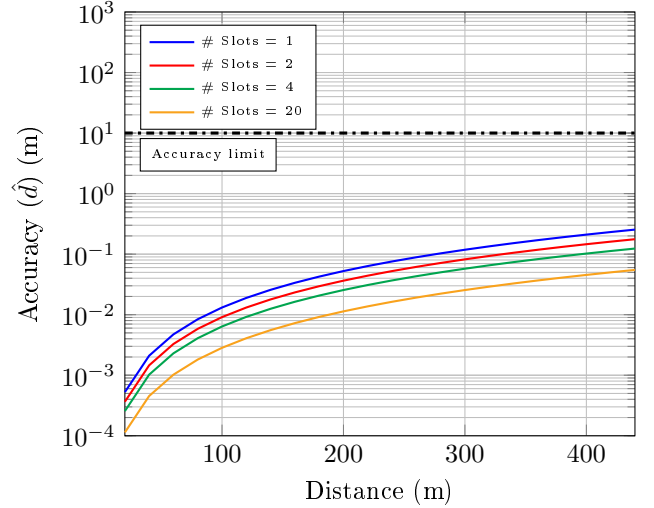
KPI	Required accuracy and confidence level
Horizontal Positioning	10 m with confidence level 90 %
Vertical Positioning	10 m with confidence level 90 %
Velocity	5 m/s with confidence level 90 %

TABLE IV: Maximum unambiguous values of the range and radial-velocity estimates for the system parameters in Table II.

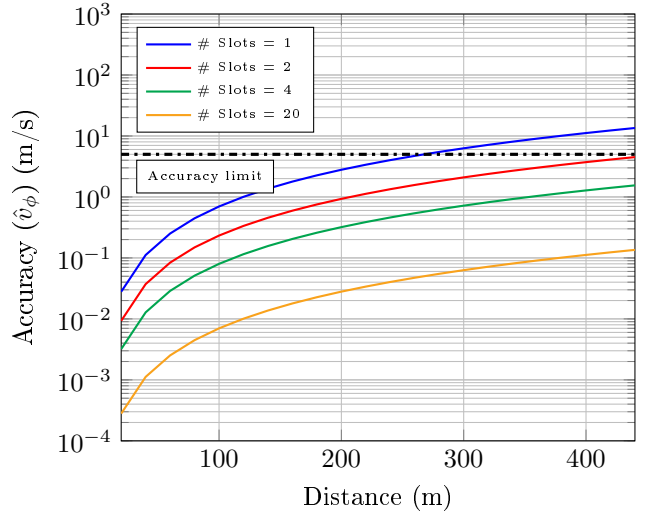
Magnitude	Maximum value
Range (d_{max})	4996.5 m
Velocity (v_ϕ^{max})	525.2 m/s

TABLE V: Resolution values of the range and radial-velocity estimates when using DFT-based estimators with N_{per} samples and the system parameters in Table II.

N_{per}	16	256	4096	65536
Δd (m)	313.3	19.52	1.220	0.076
Δv_ϕ (m/s)	65.6	4.10	0.256	0.016



(a) Highest accuracy in range estimation.



(b) Highest accuracy in radial-velocity estimation.

Fig. 4: Maximum achievable accuracy in range and radial-velocity estimations using the full-slot sensing pattern.

$K_{\text{comb}}^{\text{PRS}}$ when multiple time slots are employed. However, the accuracy strongly depends on the PRS pattern when a single time slot is used: the larger $K_{\text{comb}}^{\text{PRS}}$, the better the accuracy. The rationale for this behavior is that the radial-velocity information induces a phase shift in the received symbols, $Y_{q,m}$, which primarily varies with the symbol index m , as shown in (22), and the time extent of the PRS pattern increases with $K_{\text{comb}}^{\text{PRS}}$, as illustrates in Fig. 2. This can also be explained in terms of the CRLB in (11), which shows that the performance improves with increasing variance of the indices of the OFDM symbols used in the estimation, and the latter increases with $K_{\text{comb}}^{\text{PRS}}$.

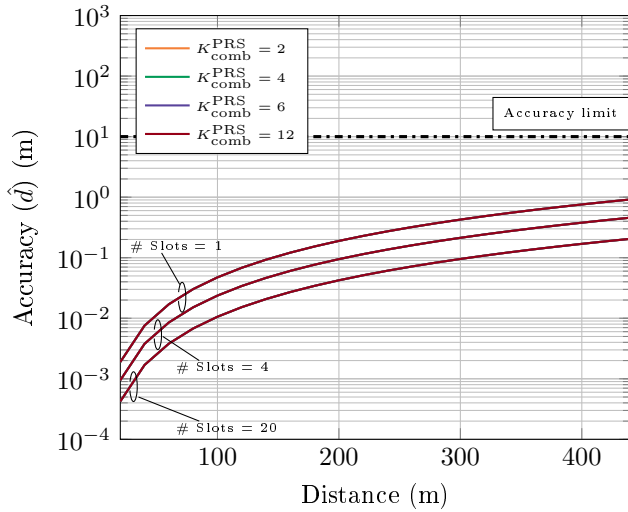
Now, the performance obtained with the proposed DDRS patterns is assessed. Fig. 6 depicts the accuracy bounds for the range and radial-velocity obtained when the DDRS resources in 1, 4 and 20 time slots are used. As observed, similar accuracy levels are obtained for all DDRS patterns. The configurations $\{M_{\text{DDRS}}, K_{\text{comb}}^{\text{DDRS}}\} = \{\{2, 2\}, \{7, 7\}, \{14, 14\}\}$

provide slightly better radial-velocity accuracy when 4 and 20 time slots are considered. In contrast, for a single time slot, the configurations $\{\{7, 7\}, \{14, 14\}\}$ achieve the best performance. Interestingly, obtained values are similar to the ones given by the PRSs when the estimation is performed using multiple time slots. When a single time slot is used, the range estimation accuracy is similar to that obtained with the PRSs, whereas the radial-velocity accuracy becomes almost independent of the DDRS pattern and matches the best-case performance of the PRS pattern obtained with $K_{\text{comb}}^{\text{PRS}} = 12$. This result is in agreement with the CRLB in (11), since the variance of the symbol indices of the PRS is very small when a single time slot is employed, but similar to that of the DDRS when multiple slots are used.

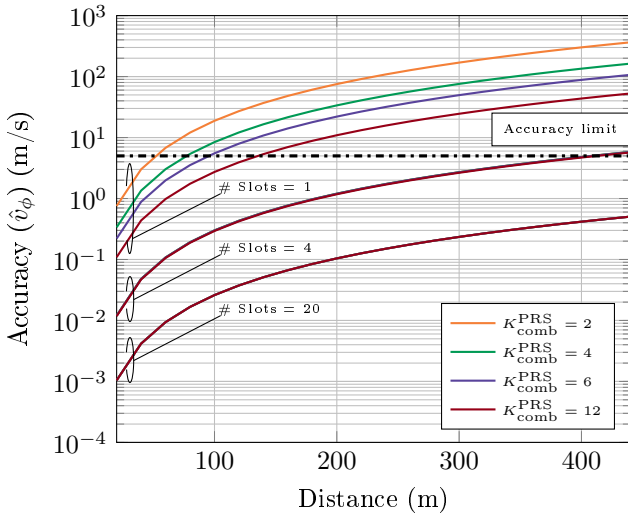
Since the accuracy values obtained from a single time slot are insufficient to meet the radial-velocity accuracy requirement in Table III, practical estimators have to resort to multiple slots.

Hence, presented results suggest that defining a new reference signal for sensing purposes may be unnecessary when the 5G frame structure is employed.

Accuracy values presented so far have been derived from the variance given by the CRLB. We now prove that the estimator proposed in Algorithm V.1 attains this bound over a wide range of distances. To this end, Fig. 7 depicts the accuracy of the range and radial-velocity estimations obtained when the full-slot sensing pattern is employed. Presented values are computed from (14) using the bias and variance of the estimates obtained by means of Monte Carlo simulations. Results are shown for STs with different radial velocities and three observation sets (1, 4, and 20 time slots). As seen, the proposed estimator is efficient over the required range of distances (up to 420 m), except for the estimates obtained using a single time slot, for which the threshold effect limits the range over which the accuracy requirement is met to a maximum of 400 m.

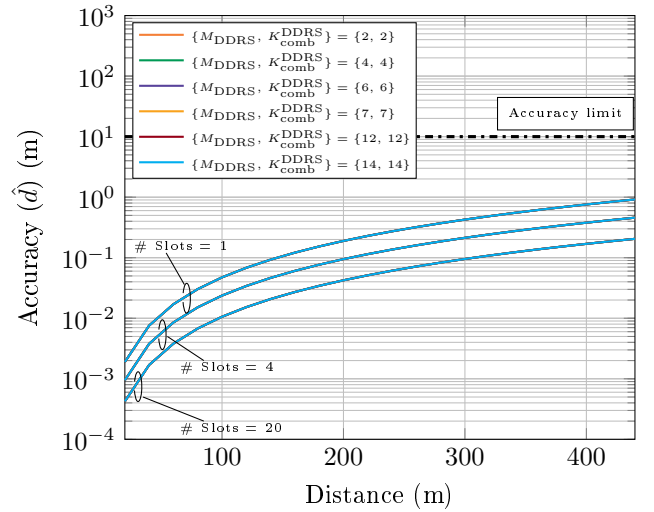


(a) Highest accuracy in range estimation.

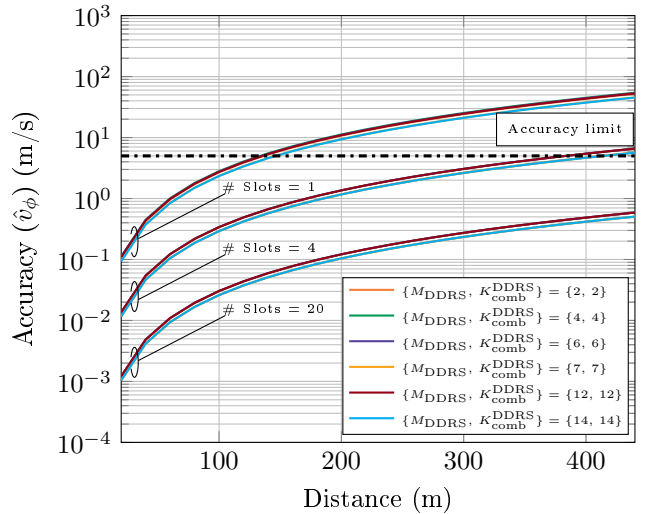


(b) Highest accuracy in radial-velocity estimation.

Fig. 5: Maximum achievable accuracy in range and radial-velocity estimations using different PRS sensing patterns.



(a) Highest accuracy in range estimation.



(b) Highest accuracy in radial-velocity estimation.

Fig. 6: Maximum achievable accuracy in range and radial-velocity estimations using different DDRS sensing patterns.

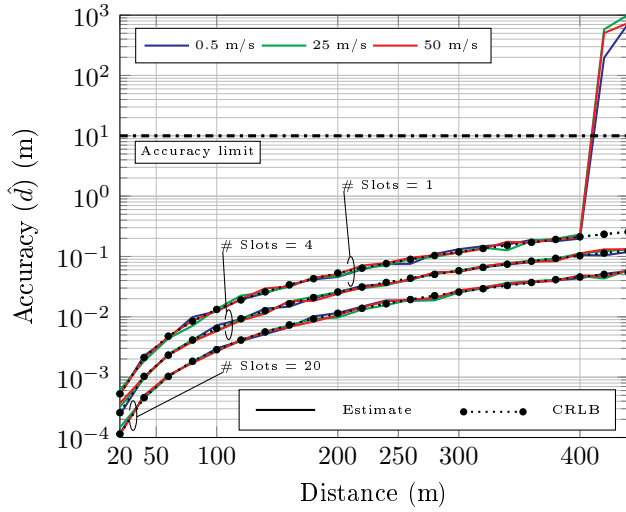
Finally, to highlight the improvement of the proposed two-step iterative estimator over plain ML ones, Fig. 8 shows the accuracy achieved by the latter, as defined in the paragraph immediately following (24), when using the full-slot sensing pattern for velocity estimation, whereas a single slot suffices to satisfy the accuracy requirement for range estimation.

VII. CONCLUSION

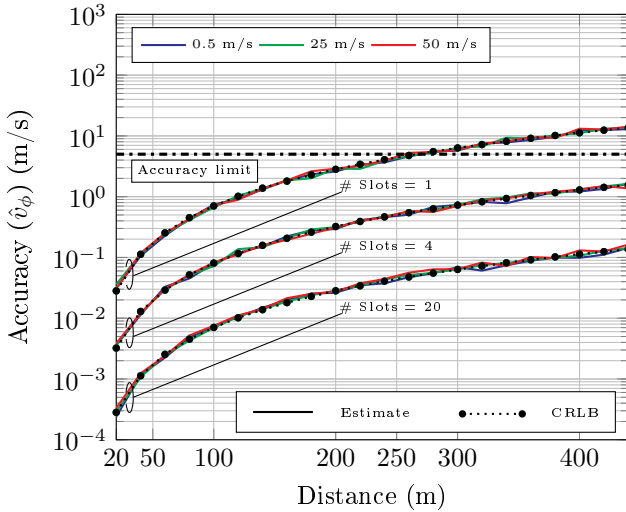
This work has determined the theoretical accuracy limits for range and velocity estimation of a single UAV using 5G signals within a monostatic sensing framework. The compact CRLB expressions derived herein highlight the fundamental trade-offs between estimation accuracy and system parameters. These variance bounds are then translated into accuracy values and compared with the requirements specified by the 3GPP. The

obtained results indicate that, when all the resources within a slot are used for sensing purposes, the estimator must exploit information from at least two slots to meet the accuracy limit for velocity estimation, whereas a single slot suffices to satisfy the accuracy requirement for range estimation.

The accuracy achieved using the 5G NR PRS, which is the most suitable standardized reference signal for sensing purposes, is also evaluated and compared with that obtained using a reference signal specifically designed for sensing. The presented results show that, when estimation is performed over the PRS resources of a single slot, the most suitable PRS pattern is the one with a comb size equal to 12, $K_{\text{comb}}^{\text{PRS}} = 12$. However, negligible differences between patterns are observed when estimation is carried out over multiple slots. Furthermore, since it has also been shown that more than four slots are required to meet the radial-velocity accuracy requirements imposed by the 3GPP, in practice, this implies that the PRS yields nearly the same

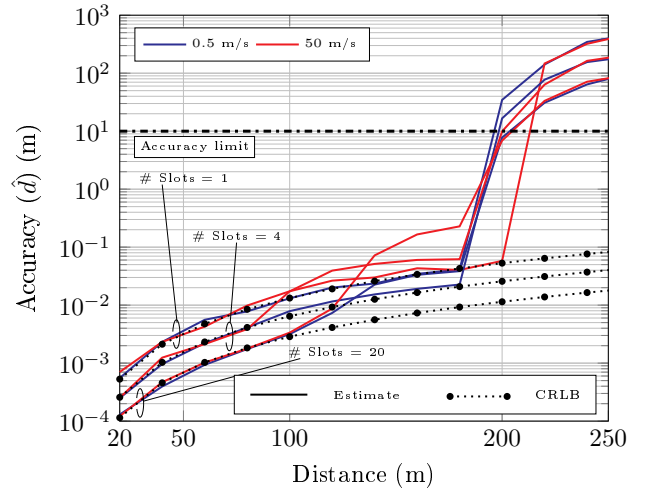


(a) Accuracy obtained when estimating the range using the proposed two-step iterative algorithm.

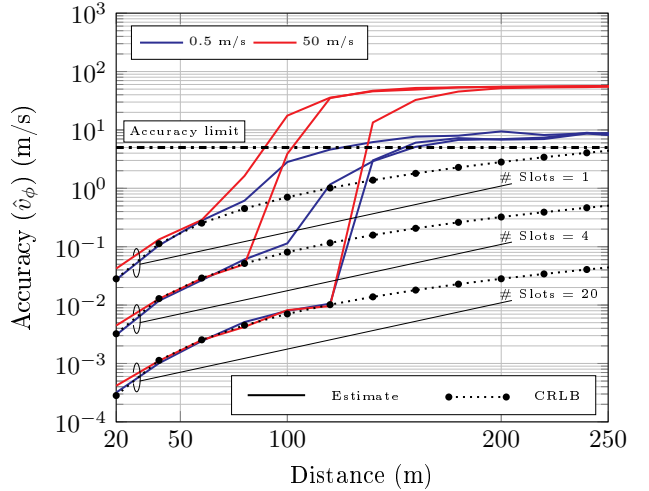


(b) Accuracy obtained when estimating the radial-velocity using the proposed two-step iterative algorithm.

Fig. 7: Accuracy obtained when estimating the radial-velocity using the proposed two-step iterative algorithm and the full-slot sensing pattern.



(a) Accuracy obtained when estimating the range using a plain ML estimator.



(b) Accuracy obtained when estimating the radial-velocity using a plain ML estimator.

Fig. 8: Accuracy of the range and radial-velocity estimation obtained with plain ML estimators and the full-slot sensing pattern.

accuracy as specifically designed signals, which outperform it in single-slot estimation.

Although, in principle, there is no guarantee that a practical estimator attaining the CRLB can be designed, we propose a two-step iterative range and radial-velocity estimator that is efficient over a significantly wider range of distances than conventional maximum-likelihood (ML) estimators. The presented results show that the latter are strongly affected by the well-known threshold effect, which limits the distance range over which the accuracy requirements imposed by the 3GPP are satisfied to less than 200 m for range estimation and less than 130 m for radial-velocity estimation.

REFERENCES

- [1] D. Zhang, Y. Cui, X. Cao, N. Su, Y. Gong, F. Liu, W. Yuan, X. Jing, J. Andrew Zhang, J. Xu, C. Masouros, D. Niyato, and M. Di Renzo, "Integrated sensing and communications over the years: An evolution perspective," *IEEE Communications Surveys & Tutorials*, vol. 28, pp. 5014–5048, 2026.
- [2] H. Andersson, "Joint communication and sensing in 6G networks." Ericsson Blog, [On-line, 24/03/2026] <https://www.ericsson.com/en/blog/2021/10/joint-sensing-and-communication-6g>, 2021.
- [3] Y. Li, F. Liu, Z. Du, W. Yuan, and C. Masouros, "ISAC-Enabled V2I Networks Based on 5G NR: How Much Can the Overhead Be Reduced?," in *IEEE International Conference on Communications Workshops (ICC Workshops)*, pp. 691–696, 2023.
- [4] Y. Cui, J. Nie, and F. e. a. Liu, "Integrated sensing and communication: Towards multifunctional perceptive network," *arXiv preprint arXiv:2510.14358*, 16/10/2025, 2025.
- [5] J. A. Zhang, M. L. Rahman, K. Wu, X. Huang, Y. J. Guo, S. Chen, and J. Yuan, "Enabling joint communication and radar sensing in mobile networks—a survey," *IEEE Communications Surveys & Tutorials*, vol. 24, no. 1, pp. 306–345, 2022.
- [6] 3GPP TSG RAN WG1, "Summary #5 on Evaluations for NR ISAC RAN WG1 #122bis, Agenda Item 10.5.1, Moderator: Xiaomi," RAN WG1 Meeting Contribution R1-2507427, Third Generation Partnership Project (3GPP), Prague, Czech, Nov. 2025. https://www.3gpp.org/ftp/tsg_ran/WG1_RL1/TSGR1_122b/Docs.
- [7] I. Bekkerman and J. Tabrikian, "Target detection and localization using MIMO radars and sonars," *IEEE Transactions on Signal Processing*, vol. 54, no. 10, pp. 3873–3883, 2006.
- [8] L. Gaudio, M. Kobayashi, B. Bissinger, and G. Caire, "Performance Analysis of Joint Radar and Communication using OFDM and OTFS," in *IEEE International Conference on Communications Workshops (ICC Workshops)*, pp. 1–6, 2019.
- [9] F. Liu, Y.-F. Liu, A. Li, C. Masouros, and Y. C. Eldar, "Cramér-rao bound optimization for joint radar-communication beamforming," *IEEE Transactions on Signal Processing*, vol. 70, pp. 240–253, 2022.
- [10] Z. Wei, Y. Wang, L. Ma, S. Yang, Z. Feng, C. Pan, Q. Zhang, Y. Wang, H. Wu, and P. Zhang, "5G PRS-Based Sensing: A Sensing Reference Signal Approach for Joint Sensing and Communication System," *IEEE Transactions on Vehicular Technology*, vol. 72, no. 3, pp. 3250–3263, 2023.
- [11] M. Soltani, M. Mirmohseni, and R. Tafazolli, "On stochastic fundamental limits in a downlink integrated sensing and communication network," *IEEE Transactions on Communications*, vol. 73, no. 11, pp. 10436–10450, 2025.
- [12] 3GPP TSG RAN WG1, "Summary #6 on Evaluations for NR ISAC RAN WG1 #123, Agenda Item 10.5.1, Moderator: Xiaomi," RAN WG1 Meeting Contribution R1-2509243, Third Generation Partnership Project (3GPP), Dallas, US, Nov. 2025. https://www.3gpp.org/ftp/tsg_ran/WG1_RL1/TSGR1_123/Docs.
- [13] J. G. Proakis and M. Salehi, *Digital Communications*. New York, NY, USA: McGraw-Hill, 5th ed., 2008.
- [14] C. Sturm and W. Wiesbeck, "Waveform design and signal processing aspects for fusion of wireless communications and radar sensing," *Proceedings of the IEEE*, vol. 99, no. 7, pp. 1236–1259, 2011.
- [15] X.-Y. Wang, S. Yang, K. Meng, H.-Y. Zhai, and C. Masouros, "On the Fundamental Trade-Offs of Time-FrequencyResource Distribution in OFDMA ISAC," *arXiv:2407.12628*, 2024.
- [16] "Third Generation Partnership Project; Technical Specification Group Radio Access Network; NR; Base Station (BS) radio transmission and reception (Release 19)," 3GPP Technical Specification TS 38.104, Third Generation Partnership Project (3GPP), June 2025. Available at https://www.3gpp.org/ftp/Specs/archive/38_series/38.104/.
- [17] "5G; NR; Physical channels and modulation," Technical Specification TS 38.211, E.T.S.I., July 2025. Available at https://portal.etsi.org/webapp/workprogram/Report_WorkItem.asp?WKI_ID=75300.
- [18] E. Dahlman, S. Parkvall, and J. Sköld, *5G NR: The Next Generation Wireless Access Technology*. Elsevier, 2018.
- [19] S. M. Kay, *Fundamentals of Statistical Signal Processing: Estimation Theory*. USA: Prentice Hall, Inc., 1993.
- [20] A. Steinhardt and C. Bretherton, "Thresholds in frequency estimation," in *IEEE International Conference on Acoustics, Speech, and Signal Processing*, vol. 10, pp. 1273–1276, 1985.
- [21] D. Rife and R. Boorstyn, "Single tone parameter estimation from discrete-time observations," *IEEE Transactions on Information Theory*, vol. 20, no. 5, pp. 591–598, 1974.
- [22] Third Generation Partnership Project (3GPP), "Study on channel model for frequencies from 0.5 to 100 GHz," Technical Report TR 38.901 V19.1.0, 3GPP Technical Specification Group Radio Access Network, Sept. 2025. (Release 19).
- [23] 3GPP TSG RAN WG1, "Summary #4 on Evaluations for NR ISAC RAN WG1 #122, Agenda Item 10.5.1, Moderator: Xiaomi," RAN WG1 Meeting Contribution R1-2506479, Third Generation Partnership Project (3GPP), Bengaluru, India, 2025. https://www.3gpp.org/ftp/tsg_ran/WG1_RL1/TSGR1_122/Docs.